


**Chaos onset in large rings of Bose-Einstein condensates**Damian Wozniak <sup>1,2</sup>, Johann Kroha <sup>3</sup>, and Anna Posazhennikova<sup>1</sup><sup>1</sup>*Institut für Physik, Universität Greifswald, 17487 Greifswald, Germany*<sup>2</sup>*Department of Physics, Royal Holloway, University of London, Egham, Surrey TW20 0EX, United Kingdom*<sup>3</sup>*Fachbereich Physik, Universität Bonn, 53115 Bonn, Germany*

(Received 1 December 2021; accepted 16 August 2022; published 16 September 2022)

We consider large rings of weakly coupled Bose-Einstein condensates, analyzing their transition to chaotic dynamics and loss of coherence. Initially, a ring is considered to be in an eigenstate, i.e., in a commensurate configuration with equal site fillings and equal phase differences between neighboring sites. Such a ring should exhibit a circulating current whose value will depend on the initial, nonzero phase difference. The appearance of such currents is a signature of an established coherence along the ring. If phase difference falls between  $\pi/2$  and  $3\pi/2$  and interparticle interaction in condensates exceeds a critical interaction value  $u_c$ , the coherence is supposed to be quickly destroyed because the system enters a chaotic regime due to inherent instabilities. This is, however, only part of the story. It turns out that chaotic dynamics and resulting averaging of circular current to zero are generally offset by a critical timescale  $t_c$ , which is almost two orders of magnitude larger than the one expected from the linear stability analysis. We study the critical timescale in detail in a broad parameter range.

DOI: [10.1103/PhysRevA.106.033316](https://doi.org/10.1103/PhysRevA.106.033316)**I. INTRODUCTION**

Ring-coupled Bose-Einstein condensates with an initially finite phase difference between neighboring sites constitute a particularly interesting system. They allow for circulating currents, which results in the controlled formation of topological defects such as vortices. Possible applications of such systems range from interferometry [1,2] to quantum computation, atomtronics, and superconducting quantum interference devices [3–7].

A while ago, a ring of three condensates was studied in the whole range of initial phase differences between neighboring sites [8,9] with the goal of finding the probability of vortex generation via the Kibble-Zurek mechanism in nonuniform, domain-structured superfluids. Experimentally, the idea was tested by three <sup>87</sup>Rb condensates merging, which indeed led to the formation of vortices, whose number strongly depended on the merging velocity [10].

Although in a ring of three coupled condensates, circular current can be nonzero when all three phase differences differ from each other, the maximum value of the circular current is reached only for the commensurate case, i.e., when all three phase differences are the same [8]. This is because only a commensurate case corresponds to an eigenstate of the system. Importantly, this circular current depends on the system parameters, in particular on the interaction between condensed particles. Linear stability analysis provides a critical interaction value  $u_c$ , above which some of the eigenmodes become unstable and chaotic dynamics sets in for  $u > u_c$ . The time-averaged circular current gradually tends to zero as the interaction increases apart from the remaining sharp peaks associated with the eigenmodes [8]. It is therefore not clear why nonzero circular currents are still present for  $u \gg u_c$  in the numerical results of Ref. [8].

Further studies on condensate rings (with number of sites  $N_s \geq 3$ ) investigated different theoretical aspects, including dynamical and thermodynamical stability [11,12], chaos and ergodicity [13–15], symmetry analysis and effects of quantum many-body dynamics [16], and quantum quenches [17]. However, in those works, the values of the circular currents were not investigated in detail in the chaotic regime, and timescales associated with the currents were not discussed.

From an experimental point of view, it is rather challenging to realize circulating currents in large rings and for large winding numbers due to their quick decay to flows with lower winding numbers (see, for instance, experiments on <sup>87</sup>Rb annular condensates in Ref. [18]). Recently, substantial progress in the creation of stable superflows has been achieved in six- and seven-site rings of polaritonic condensates confined in microcavities [19]. Particularly interesting is that persistent circular currents with large winding numbers have been observed for nominally unstable initial configurations for  $N_s = 7$  and winding numbers  $k = 2$  and  $k = 3$  [19].

Motivated by these developments and open questions, we investigate how a stable, noninteracting system turns chaotic as a nonlinear interaction is turned on. We systematically study the effect of chaos on circular currents and coherence, depending on interaction, initial conditions, and system size. We show that, although chaos obstructs circular flow, it does not set in immediately even if the system is tuned to an unstable eigenmode. We identify a critical timescale associated with this type of dynamics and demonstrate how the timescale depends on the system's various parameters. We show that the timescale is much larger than the one expected from the linear stability analysis, which explains the numerical results of Ref. [8] and can provide insight into the experimental results of Ref. [19].

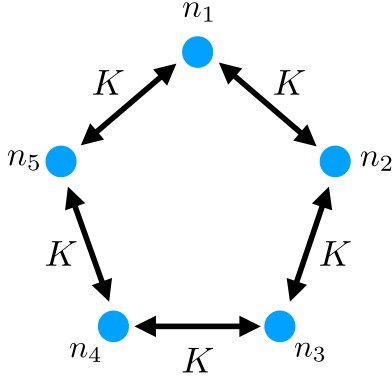


FIG. 1. Schematic setup of the ring system for five wells ( $N_s = 5$ ). Circles represent condensate wave functions,  $K$  is the Josephson coupling constant (5), and  $n_i$  are condensate populations according to (6).

This paper is organized as follows: In Sec. II we formulate the model and derive equations of motion and the expression for circular current. In Sec. III we analyze the circular current in the noninteracting system for a special case of symmetric initial conditions and show the current becomes a simple sine wave in the limit of large  $N_s$ . In Sec. IV after a brief discussion of unstable modes and characteristic interaction, we analyze the time-dependent circular current at unstable modes and identify a particular timescale  $t_c$  associated with the system transition to a chaotic regime. We show that the slide to the chaotic regime occurs exponentially and study the time-averaged circular current, showing how the current at unstable modes gradually disappears upon increasing interaction. We conclude in Sec. V.

## II. MODEL AND EQUATIONS OF MOTION

We consider a system of  $N$  condensed bosons trapped in a one-dimensional periodic potential consisting of  $N_s$  wells with periodic boundary conditions (see setup shown in Fig. 1). The average filling factor in the system

$$\rho = \frac{N}{N_s} \quad (1)$$

is assumed to be macroscopic so that the semiclassical Gross-Pitaevskii approximation is applicable for the system description (for example, in experiments on long arrays of  $^{87}\text{Rb}$  condensates  $\rho \approx 1000$  according to Ref. [20]). The local condensates are considered to be weakly linked in order for Josephson current to be induced between the sites [21]. Note that in all calculations we keep the number of particles per site  $\rho$  constant when changing the system size  $N_s$ . The general Gross-Pitaevskii equation reads

$$i\hbar \frac{\partial}{\partial t} \Psi(\mathbf{r}, t) = \left( -\frac{\hbar^2}{2m} \nabla^2 + V_{\text{ext}}(\mathbf{r}) + g|\Psi(\mathbf{r}, t)|^2 \right) \Psi(\mathbf{r}, t), \quad (2)$$

where  $\Psi(\mathbf{r}, t)$  is the mean-field averaged bosonic field operator  $\langle \hat{\Psi}(\mathbf{r}, t) \rangle$ ,  $V_{\text{ext}}(\mathbf{r})$  is the multiwell external potential, and  $g$  is a repulsive contact interaction constant. By expanding the semiclassical wave function in terms of a set of localized basis

functions [Wannier functions  $\phi_i(\mathbf{r})$ ],

$$\Psi(\mathbf{r}, t) = \sum_{i=1}^{N_s} \phi_i(\mathbf{r}) \psi_i(t), \quad (3)$$

and integrating out the spatial degrees of freedom, we obtain the standard discrete nonlinear Schrödinger equations (DNLSEs) for  $\psi_i$  [22]:

$$i\hbar \frac{\partial}{\partial t} \psi_i(t) = [E_i + U_i |\psi_i(t)|^2] \psi_i(t) - K_{i,i-1} \psi_{i-1}(t) - K_{i,i+1} \psi_{i+1}(t), \quad i = 1, 2, \dots, N_s. \quad (4)$$

The periodic boundary conditions imply  $N_s + 1 \rightarrow 1$ . DNLSs adequately capture the dynamics of multiple coupled condensates, which was verified in experimental work [20]. The model parameters in Eq. (4), the zero-point energies  $E_i$ , on-site interaction  $U_i$ , and Josephson couplings between neighboring wells  $K_{i,i\pm 1}$  are given by [21]

$$E_i = \int d\mathbf{r} \left[ \frac{\hbar^2}{2m} |\nabla \phi_i(\mathbf{r})|^2 + |\phi_i(\mathbf{r})|^2 V_{\text{ext}}(\mathbf{r}) \right],$$

$$U_i = g \int d\mathbf{r} |\phi_i(\mathbf{r})|^4,$$

$$K_{i,i\pm 1} = - \int d\mathbf{r} \left[ \frac{\hbar^2}{2m} \nabla \phi_i(\mathbf{r}) \nabla \phi_{i\pm 1}(\mathbf{r}) + \phi_i(\mathbf{r}) V_{\text{ext}}(\mathbf{r}) \phi_{i\pm 1}(\mathbf{r}) \right]. \quad (5)$$

We make use of the ansatz

$$\psi_i(t) = \sqrt{n_i(t)} e^{i\theta_i(t)}, \quad (6)$$

where we introduced the site populations  $n_i$  normalized by the filling factor  $\rho$ ,

$$n_i(t) = \frac{N_i(t)}{\rho}, \quad (7)$$

where  $N_i(t)$  is the number of particles in the condensate on site  $i$  at time  $t$ . Thus, an initially homogeneous distribution of atoms means  $n_i(0) = 1$  for all  $i$ . With that Eq. (4) can be rewritten as a set of differential equations for  $n_i$  and phase differences  $\theta_{i,i+1} = \theta_{i+1} - \theta_i$  as follows:

$$\dot{n}_i = -2\sqrt{n_i}(\sqrt{n_{i+1}} \sin \theta_{i,i+1} - \sqrt{n_{i-1}} \sin \theta_{i-1,i}),$$

$$\dot{\theta}_{i,i+1} = u(n_i - n_{i+1}) + \left( \sqrt{\frac{n_i}{n_{i+1}}} - \sqrt{\frac{n_{i+1}}{n_i}} \right) \cos \theta_{i,i+1} - \sqrt{\frac{n_{i-1}}{n_i}} \cos \theta_{i-1,i} + \sqrt{\frac{n_{i+2}}{n_{i+1}}} \cos \theta_{i+1,i+2}. \quad (8)$$

In deriving these equations we assumed the following simplifications:  $E_i = 0$ ,  $U_i \equiv U$ , and  $K_{i,i+1} \equiv K$  for all values of  $i$ . We also expressed the time argument  $t$  in units of  $\hbar/K$  and introduced the dimensionless interaction parameter

$$u = \frac{U\rho}{K}. \quad (9)$$

These equations conserve  $\sum_i n_i = N_s$  and the total energy

$$E = \frac{\rho K}{\hbar} \left( \frac{u}{2} \sum_i n_i^2 - 2 \sum_i \sqrt{n_i n_{i+1}} \cos \theta_{i,i+1} \right). \quad (10)$$

We define the circular current as the average current in a clockwise loop around the ring of condensates

$$I = \frac{1}{N_s} \sum_{i=1}^{N_s} I_{i,i+1}, \quad (11)$$

where  $I_{i,i+1}$  is the particle current from site  $i$  to  $i+1$  defined as

$$I_{i,i+1} = 2 \operatorname{Im}[\psi_i^*(t)\psi_{i+1}(t)] = 2\sqrt{n_i n_{i+1}} \sin(\theta_{i,i+1}). \quad (12)$$

Note that the current defined in this way has units  $\rho K/\hbar$ . In the next section, we analyze the current analytically for  $u=0$  and a special case of initial conditions.

### III. CIRCULAR CURRENT IN THE NONINTERACTING CASE

The noninteracting case with  $U_i=0$  and coupling constants  $K_{i,i+1} \equiv K$  can be solved exactly for any number of sites  $N_s$ , as shown in Appendix A. However, one does not need these solutions in order to calculate circular current, as it can be straightforwardly derived from the current conservation condition [one can show, for example, that  $\partial_t I = 0$  with the help of Eq. (4)]. We thus get for the circular current

$$I = I_0 = \frac{2}{N_s} \operatorname{Im} \sum_{i=1}^{N_s} \psi_i^*(0)\psi_{i+1}(0). \quad (13)$$

We see that the current is constant and the value of this constant depends on the initial  $n_i(0)$  and  $\theta_{i,i+1}(0)$ . For the homogeneous condensate distribution  $n_i(0) = 1$ , the current depends on only the initial phase differences.

We chose the following initial conditions for the phase differences:

$$\theta_{i,i+1} = \begin{cases} \theta_0 & \text{for } i = 1, \dots, N_s - 1, \\ -(N_s - 1)\theta_0 & \text{for } i = N_s, \end{cases} \quad (14)$$

so that

$$\psi_j(0) = e^{i(j-1)\theta_0}, \quad j = 1, 2, \dots, N_s. \quad (15)$$

We now get for the current in Eq. (13) the simple expression

$$I_0(\theta_0) = \frac{2}{N_s} \{(N_s - 1) \sin \theta_0 - \sin[(N_s - 1)\theta_0]\}. \quad (16)$$

Since the current is an odd function of the initial phase difference  $I_{\text{av}}^0(\theta_0) = -I_{\text{av}}^0(-\theta_0)$  and is  $2\pi$  periodic, it is sufficient to consider  $\theta_0 \in [0, \pi]$ . In Fig. 2 we plot  $I_0$  normalized by its maximum value  $(I_0)_{\text{max}} = 2$  versus  $\theta_0$  for various ring sizes. We see that the current has local maxima at discrete values of  $\theta_0$  given by

$$\theta_0^k = \frac{2\pi k}{N_s}, \quad (17)$$

where the integer  $k = 1, \dots, N_s$  has the meaning of the winding number. This result is not surprising since the discrete values  $\theta_0^k$  play the role of quantized components of the effective quasimomentum in Fourier space. Circular current at

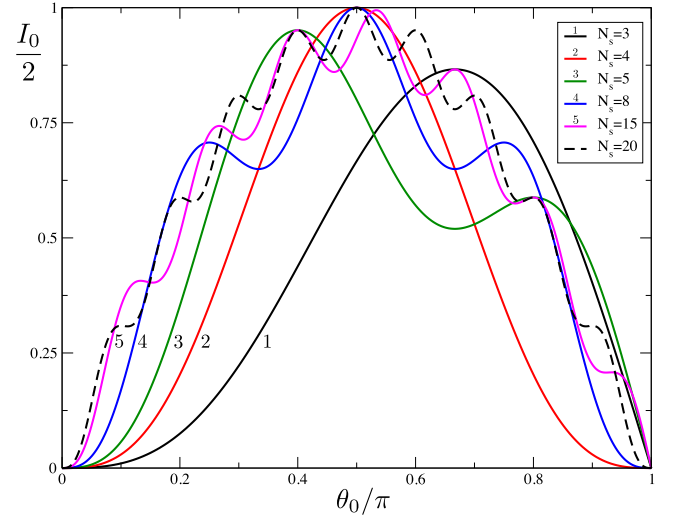


FIG. 2. Average current of the noninteracting system  $I_0$  (16) divided by its maximum value ( $=2$ ) versus initial phase difference  $\theta_0$  for initial conditions (15), plotted for condensate rings of different sizes ( $N_s = 3, 4, 5, 8, 15$ , and  $20$ ).

these values corresponds to the group velocity  $\partial E/\partial \theta_0^k$  and is reduced to  $I_0(\theta_0^k) = 2 \sin(\theta_0^k)$ . The ring system is then in an eigenstate. Curiously, in the noncommensurate case  $\theta_0 \neq \theta_0^k$  of our initial conditions, the circular current (16) is still time independent.

### IV. CIRCULAR CURRENT FOR RING-COUPLED, INTERACTING CONDENSATES

#### A. Chaotic behavior and the critical interaction

Nonzero interaction introduces nonlinearity into our system of equations, and since the dimensionality of the system is larger than three, chaotic dynamics is expected, at least in certain cases. In order to identify the parameter range when it happens, we perform the linear stability analysis of the coupled real equations (8). The stability is decided by the eigenvalues of the corresponding Jacobian matrix (see Appendix B for details). These  $2N_s$  eigenvalues can be derived analytically due to the Jacobian matrix's special, blockwise circulant structure. The eigenvalues of the Jacobian matrix at the fixed points of the system are then

$$\lambda_j(k) = 2i \left\{ -\sin \theta_0^k \sin \left( \frac{2\pi j}{N_s} \right) \pm \sin \left( \frac{\pi j}{N_s} \right) \sqrt{2 \cos \theta_0^k \left[ 2 \cos \theta_0^k \sin^2 \left( \frac{\pi j}{N_s} \right) + u \right]} \right\}, \quad (18)$$

where  $j = 1, 2, \dots, N_s$ . These eigenvalues, when divided by  $i$ , correspond to the eigenvalues of the Hamiltonian linearized around the fixed points and therefore to discrete Bogoliubov excitations. The discrete Bogoliubov spectrum was discussed previously in the context of condensate arrays [23] and the Bogoliubov–de Gennes description of a circular array of Bose–Einstein condensates [11].

The eigenvalues  $\lambda_j$  are zero or purely imaginary, and both equations in (8) are stable unless the expression under the square root turns negative. Since we consider only repulsive interactions,  $u > 0$ , the condition for at least one eigenvalue to acquire a real part is

$$\cos \theta_0^k < 0, \quad (19)$$

$$2 \cos \theta_0^k \sin^2 \left( \frac{\pi j}{N_s} \right) + u > 0. \quad (20)$$

The analysis of these inequalities provides the expression for the upper bound of interaction below which the stationary points of the nonlinear equations are still stable. The first eigenvalue acquiring a real part turns the system unstable, which first occurs for  $j = 1$ , giving us the critical interaction

$$u_c = -2 \cos \theta_0^k \sin^2 \left( \frac{\pi}{N_s} \right). \quad (21)$$

This means that our system becomes unstable without any initial perturbation, but just when the interaction is turned on and exceeds a critical value  $u_c$ .

Note that  $u_c > 0$  because of condition (19). We see that  $u_c$  depends on the initial conditions through the modes  $\theta_0^k$ , with the mode selection criterion (19). Accordingly, the range of unstable modes is defined by the interval

$$\frac{\pi}{2} < \theta_0^k < \frac{3\pi}{2} \quad \text{or} \quad N_s < 4k < 3N_s. \quad (22)$$

We will refer to such modes as ‘‘unstable discrete modes,’’ keeping in mind that they become unstable for  $u > u_c$ . Conditions similar to Eqs. (21) and (22) were also derived in Ref. [11] from the Bogoliubov–de Gennes equations. Conversely, modes in the complementary range

$$\theta_0^k \in [-\pi/2, \pi/2]$$

are stable and will be called ‘‘stable discrete modes.’’

It follows from Eqs. (21) and (22) that the maximum possible value of the critical interaction  $u_c = 1$ , and it is reached for the  $\pi$  mode of a four-site ring. Since  $u_c$  is just proportional to the corresponding cosine of the corresponding discrete mode, one can plot a universal, mode-independent graph for normalized characteristic interaction  $u_c / (-\cos \theta_0^k)$ , which we display in Fig. 3. One can see that  $u_c$  tends to zero relatively quickly with the increasing number of sites  $N_s$ . The inset shows the stability diagram, where modes denoted by open circles represent stable solutions independent of the value of  $u$  (given that only non-negative interactions are considered), whereas solid circles represent modes that become unstable for  $u > u_c$ .

The linear stability analysis introduces the instability exponent  $\alpha_0$ , given by the real part of the Jacobian eigenvalue  $\lambda_1$ ,

$$\alpha_0 \equiv \text{Re}(\lambda_1) = 2 \sin \left( \frac{\pi}{N_s} \right) \sqrt{2 |\cos \theta_0^k| [u - u_c]}. \quad (23)$$

This  $\alpha_0$  is the rate at which the circular current  $I(t)$  of a given mode  $\theta_0^k$  is expected to deviate exponentially in time from its stationary value  $I_0(\theta_0^k)$ . To be more specific, it should be  $2\alpha_0$  since the current is proportional to the product of two

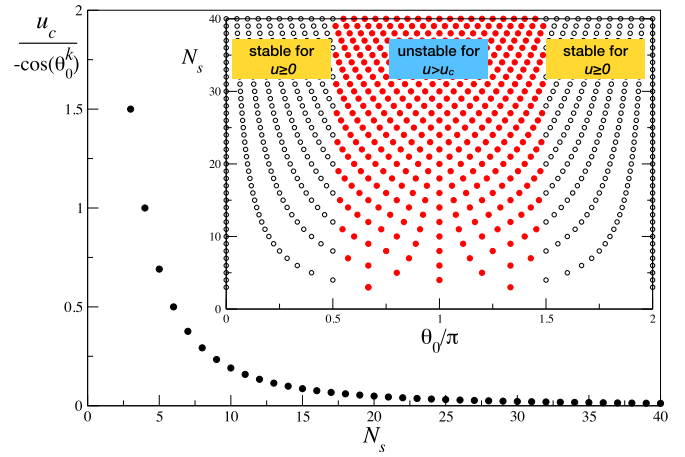


FIG. 3. Dependence of characteristic interaction  $u_c$  [divided by  $\cos(\theta_0^k)$ ] on the number of sites  $N_s$ , ranging between 3 and 40. Inset: stability diagram showing discrete modes, i.e., values of the initial phase difference  $\theta_0$  from (17) versus  $N_s$ . The modes denoted by open circles represent modes that are stable independent of the interaction  $u$  value. Discrete modes denoted by solid red circles showcase the modes which are stable for  $0 < u \leq u_c$  but become unstable for  $u > u_c$ .

condensate wave functions. Equation (23) hence establishes the deviation timescale  $\sim 1/\alpha_0$ , which would diverge at the stability boundaries, i.e., for  $\theta_0 \rightarrow \pi/2$  or  $3\pi/2$  or  $u \rightarrow u_c$ . We will show in the following section that, interestingly, chaotic behavior sets in abruptly at a much larger, critical time  $t_c \gg 1/\alpha_0$  due to the nonlinear character of the system, which is not captured by the linear stability analysis.

## B. Temporal onset of chaotic behavior

In this section, we fully characterize the decay of the unstable, discrete modes by studying the circulating current numerically beyond the linear stability analysis. Initially, the circular current has a nonzero value equal to its noninteracting value  $I_0$ , derived in Sec. III.

In Figs. 4 and 5 we show examples of the time-dependent circular current of the interacting system defined in Eqs. (11) and (12) for rings of  $N_s = 5$  and  $N_s = 20$  condensates, respectively. For  $N_2 = 5$ , according to Eq. (22), there are only two unstable modes,  $k = 2$  and  $k = 3$ . These modes are symmetric with respect to inflection at  $\theta_0 = \pi$  (see the inset in Fig. 3), and therefore, the critical value of interaction  $u_c$  is the same for both of the modes,  $u_c \approx 0.56$ . In Fig. 4 we consider three values of interaction, which are all greater than  $u_c$ :  $u = 0.6$ ,  $u = 1.2$ , and  $u = 2.4$ , and we therefore expect the current to behave chaotically in all three cases, which is indeed observed. However, chaos sets in at a certain time  $t_c > 0$  which strongly depends on the interaction  $u > u_c$ . One can see that  $t_c$  decreases as the interaction increases. For example, for  $u$  close to  $u_c$  (top panel),  $t_c$  is about 112; for  $u = 2.4$  it is about 15.

To find out whether  $t_c$  has a mode dependence, we consider in Fig. 5 a larger ring of  $N_s = 20$ . It has nine discrete, unstable modes whose critical interaction strengths  $u_c$  are listed in Table I. The circular currents are shown for different values

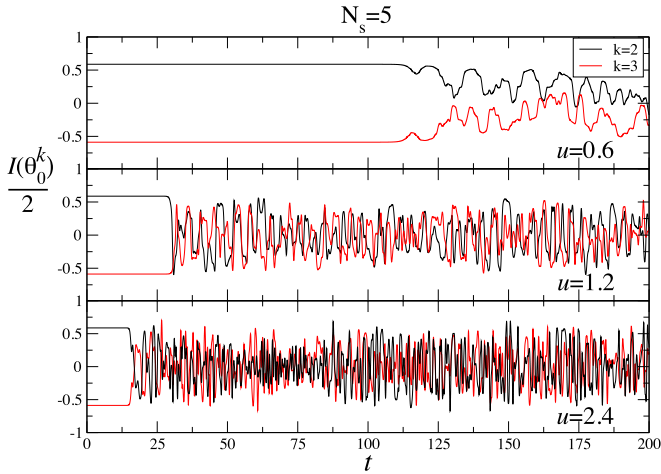


FIG. 4. Time-dependent circular current (11) for homogeneous initial conditions:  $N_s = 5$ ,  $\theta_0 = \theta_0^k$ . The black upper line in each panel is for  $k = 2$ , whereas the red lower line is for  $k = 3$ . The current is calculated numerically for three different values of dimensionless interaction  $u$ , as shown in the panels. Time  $t$  is in units of  $\hbar/K$ .

of  $u$ , all greater than the respective  $u_c$ . We observe that  $t_c$  depends not only on  $u$  but also on the mode. For example, for  $u = 3$  values of  $t_c$  of the “outer” modes ( $k = 6$  and  $k = 14$ ) are clearly greater than  $t_c$  for other modes.

In order to quantify the onset of chaos, we show in Fig. 6 the time evolution of the deviation of the circular current  $I(t)$  from its noninteracting value  $I_0(\theta_0^k) \equiv I_0$  on a logarithmic scale. As expected from the linear stability analysis, this deviation is initially exponential in time, and thus, initially the current deviation remains exponentially small, too small to resolve in the linear plots in Figs. 4 and 5.

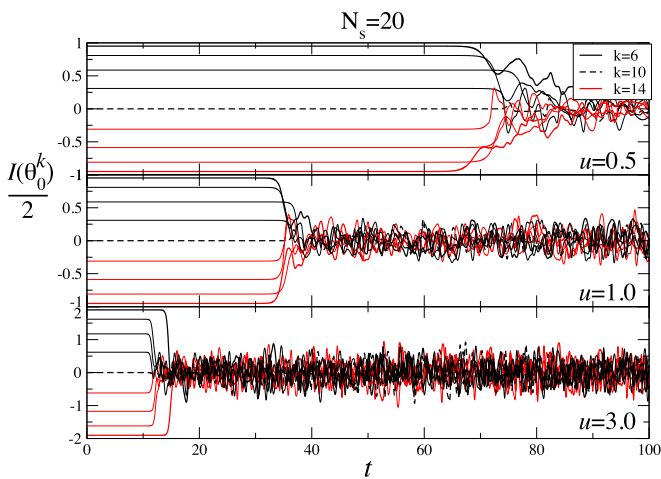


FIG. 5. Time-dependent circular current  $I(\theta_0^k)$  of the unstable modes  $6 \leq k \leq 14$  for  $N_s = 20$ . The modes are counted from top to bottom, so that the uppermost black line corresponds to  $k = 6$ , the dashed line corresponds to  $k = 10$ , and the lowermost red line corresponds to  $k = 14$ . The current is calculated numerically for three different values of  $u$ , as shown in the panels. Time  $t$  is in units of  $\hbar/K$ .

TABLE I. Values of characteristic interaction  $u_c$  for different modes  $\theta_0^k$  for the case of  $N_s = 20$ .

	$k$				
	6, 14	7, 13	8, 12	9, 11	10
$u_c$	0.015	0.029	0.040	0.047	0.049

The exponential behavior of the deviation is governed by two parameters,  $\alpha$  and  $b$ ,

$$\Delta I(t) \equiv |I_0 - I(t)|/2 = e^{\alpha t + b}, \quad (24)$$

which can be determined from linear fits to the logarithmic plot within the exponential time range (see dashed lines in Fig. 6). The comprehensive analysis for a wide range of system parameters  $u \in [0.5, 10]$  and initial conditions  $\theta_0^k \in [0, \pi]$  shows that the coefficient  $b$  has no systematic dependence on system parameters, with an average value of  $\langle b \rangle \approx -72.34$  and a standard deviation of  $\Delta b \approx 1.51$ . Furthermore, from Fig. 6 and similar plots for the wide parameter range mentioned above (not shown), we find that chaotic behavior, i.e., deviation from the exponential time evolution, sets in abruptly when the normalized current deviation  $\Delta I(t)$  reaches a universal value of about  $\ln[\Delta I(t_c)] \equiv \lambda = -2$ . This defines, via Eq. (24), the critical time for onset of chaos as

$$t_c \approx \frac{\lambda - b}{\alpha} \approx \frac{70}{\alpha}. \quad (25)$$

It shows that both the initial exponential deviation and the onset of chaotic evolution are controlled by the instability exponent  $\alpha$  alone, where, however, the critical time  $t_c$  is a factor of 70 larger than the exponential timescale  $1/\alpha$ . We note that similar long-time coherent evolution with abrupt chaos onset was found in single Bose-Josephson junctions [24]. Chaotic dynamics was induced by a highly nonlinear process of quasi-particle creation in the initially fully condensed system. A late chaos onset was also discussed in Ref. [15], where it

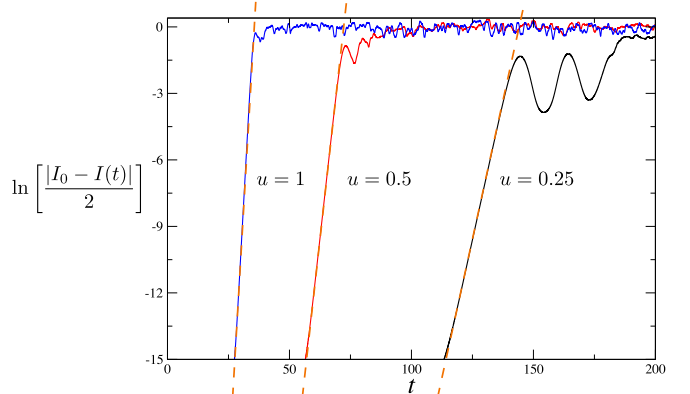


FIG. 6. Logarithmic plot of the deviation of the current from its initial value  $I_0$  versus time for  $N_s = 20$ ,  $k = 6$ , and three different values of  $u$ . Time  $t$  is in units of  $\hbar/K$ . Dashed lines are linear fits of linear parts of the graphs with intercept  $b$  and slope  $\alpha$ :  $\alpha \approx 0.5$ ,  $b \approx -71.62$  for  $u = 0.25$ ;  $\alpha \approx 0.98$ ,  $b \approx -70.55$  for  $u = 0.5$ ; and  $\alpha \approx 1.98$ ,  $b \approx -71.62$  for  $u = 1$ .

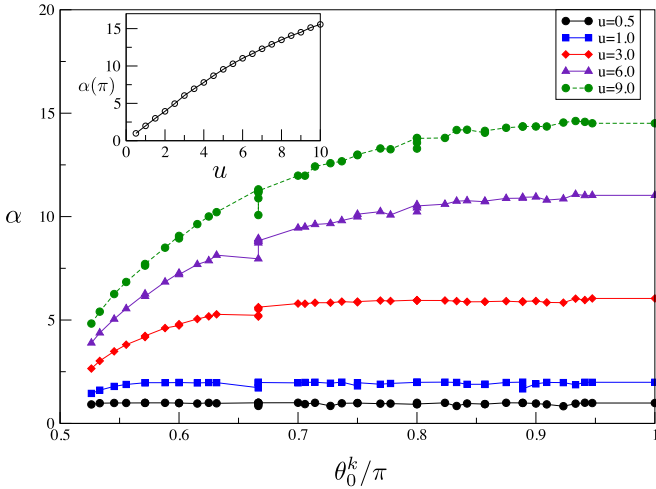


FIG. 7. The exponent  $\alpha$  versus initial  $\theta_0^k$  for different values of  $u$ . The inset shows the dependence of the maximum value of  $\alpha$ , equal to  $\alpha(\theta_0^k = \pi)$ , on  $u$ .

was attributed to a web of nonlinear resonances between the Bogoliubov frequencies.

The observed dependence of  $t_c$  (see Figs. 4 and 5) on system parameters enters through the dependence of  $\alpha$ , which we explore next. In Fig. 7 we show the results of the numerical evaluation of  $\alpha$  depending on initial mode  $\theta_0^k$  and interaction  $u$ . The plot contains data for various  $N_s$ ,  $k$ , and interaction  $u$ . Short vertical lines of data at  $\theta_0^k = 2\pi/3 \approx 0.666\pi$  correspond to rings with  $N_s = 3, 6, 9, \dots$  because they all have such a mode. However, the dependence of a particular mode on  $N_s$  is very weak, so we neglect it in the discussion and analysis. As expected,  $\alpha$  tends to zero for  $\theta_0^k \rightarrow \pi/2$  since this value of  $\theta_0^k$  marks the stability boundary (see the stability diagram in Fig. 3). Away from the stability boundary, i.e., close to  $\pi$  modes,  $\alpha$  has a weaker dependence on  $\theta_0^k$  and is significantly dependent on  $u$ . This dependence is approximately linear, as shown in the inset:  $\alpha(\pi) \approx 2u$  on the interval  $u \in (u_c, 5)$ , with  $u_c \ll 1$  in this case. For small  $u$ ,  $\alpha$  tends to zero; that is, the modes become stable.

At this point, it is interesting to compare the numerically estimated  $\alpha$  with the analytical value from (23). It turns out that the agreement holds only for small rings ( $N_s = 3$ ,  $N_s = 4$ ), whereas for larger rings the agreement with this relation quickly degrades and holds only in the close vicinity of  $u_c$ . This defines the applicability of linear stability analysis in our systems: essentially only in the vicinity of  $u_c$ . The numerical  $\alpha$  is generally larger than the approximate, analytically determined value.

Coming back to the chaos onset time  $t_c$ , as expected, it becomes arbitrarily large in two cases: close to stability boundaries in terms of the initial phase difference, i.e., close to  $\theta_0 = \pi/2$  and  $\theta_0 = 3\pi/2$ , and for interactions close to  $u_c$ . This can be seen in Fig. 8, where we present numerically calculated  $t_c$  as a function of  $u$  for a broad range of initial conditions  $\theta_0^k$ , in particular, for all unstable modes  $\theta_0^k \in (\pi/2, \pi]$  of all rings between  $N_s = 3$  and  $N_s = 20$ . To not overload the graph with information, we color-coded curves according to their initial conditions split into intervals of  $\theta_0$ : black corresponds to  $\theta_0^k \in [0.8\pi, \pi]$ , closest to the antiphase

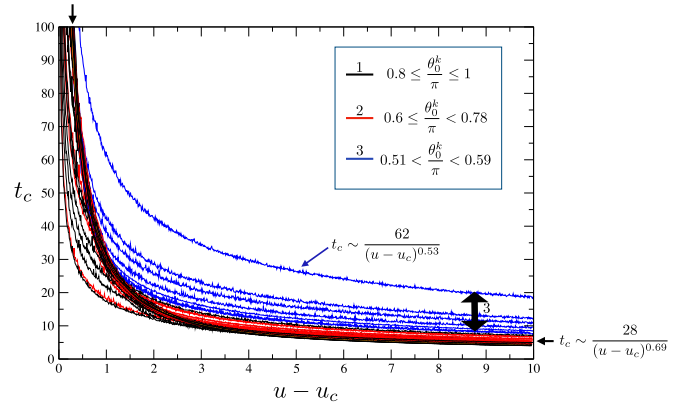


FIG. 8. Dependence of the onset of chaotic behavior  $t_c$  on interaction  $u$  measured from  $u_c$  for all unstable discrete modes in the interval  $(\pi/2, \pi]$  for  $3 \leq N_s \leq 20$ . The uppermost curve is for  $N_s = 47$  and  $k = 12$  (this amounts to  $\theta_0 \approx 0.511\pi$ ). Initial conditions are specified by  $\theta_0^k$ , and curves are split into groups depending on whether they are close to  $\pi/2$  or to  $\pi$ : black curves correspond to the values of  $\theta_0^k$  in region 1 close to  $\pi$ , red curves correspond to region 2 and  $0.6\pi < \theta_0^k < 0.78\pi$ , and the blue curves (the set of upper curves marked by the double arrow) correspond to region 3 and  $\theta_0^k$  close to  $\pi/2$ .

mode and farthest from the stable modes. One can see that most of them (in particular those with small  $u_c$ ) bunch around the curve marked by the black arrows. The marked curve is easily fit with a two-parameter fitting function resulting in  $t_c \approx 28/(u - u_c)^{0.69}$ . Red curves represent the next interval  $\theta_0^k \in [0.6\pi, 0.78\pi)$ . They start to deviate from the black curves, especially for large  $u$ . This can be better seen in Fig. 9, where we plot  $t_c^{-1}$  versus  $u - u_c$ . Last, the blue curves span the interval of  $\theta_0^k \in [0, 0.59\pi]$ . One curve is calculated for  $N_s = 47$  and  $k = 12$ , which is an example of a curve relatively close to the  $\pi/2$  mode with  $\theta_0^k \approx 0.511$  (this is the

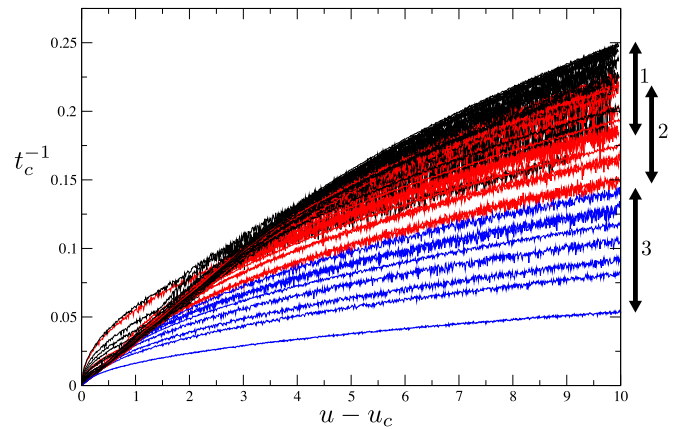


FIG. 9. Dependence of the inverse onset of chaotic behavior  $t_c^{-1}$  on interaction  $u - u_c$  for all unstable modes in the interval  $(\pi/2, \pi]$  for  $3 \leq N_s \leq 20$ . The lowest curve is for  $N_s = 47$  and  $k = 12$ . The curves are color-coded according to initial conditions in the same way as in Fig. 8. The double arrows with numbers mark the widths of the corresponding regions described in Fig. 8 for  $u - u_c = 10$ . One can clearly see the overlap between regions 1 and 2.

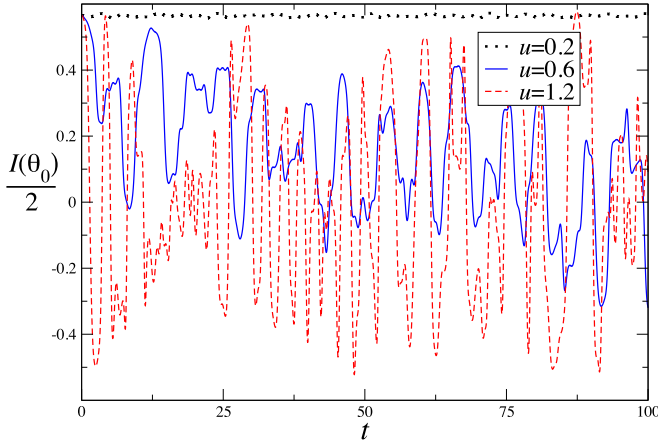


FIG. 10. Current oscillations with time for initial conditions  $\theta_0 = 0.75\pi$  and  $N_s = 20$ , i.e., for a noneigenmode. The results are shown for three different values of dimensionless interaction  $u$  shown in the legend. Time  $t$  is in units of  $\hbar/K$ .

uppermost curve in the graph). The fitting of this curve results in  $t_c \approx 62/(u - u_c)^{0.53}$ , leading to a sizable  $t_c$  even for large values of  $u$ .

Note that  $t_c$  can be determined differently, for example, from the deviation from its initial value by 0.0001 of any site occupation. Finding  $t_c$  from site occupation would lower the  $t_c$  of all of Fig. 8 about an average of 10%, which does not change any conclusions or analysis.

To get an idea of how large  $t_c$  can be in terms of experimental values, we translate the value  $t_c = 100$  to milliseconds from experimental data on arrays of condensates [20]. For example, from experiments on long arrays of cold atoms ( $N_s = 200$ ), we take the value of Josephson coupling  $K \sim 0.07E_R$ , where  $E_R$  is the recoil energy of a  $^{87}\text{Rb}$  atom of mass  $m$  absorbing one of the lattice photons

$$E_R = \frac{\hbar^2}{2m\lambda^2} \sim 1.5 \times 10^{-11} \text{ eV}, \quad (26)$$

with  $\lambda = 795 \times 10^{-9} \text{ m}$  [20]. This gives us the value of  $K \sim 1.05 \times 10^{-12} \text{ eV}$ . From this analysis it follows that the dimensionless  $t_c = 100$  will correspond to 62.86 ms. Such values of  $t_c$  could be achievable for very weak interactions, which follows from Fig. 8.

Note that when initial conditions fall in between the eigenmodes, one expects time-dependent current, as shown in Fig. 10 for  $\theta_0 = 0.75\pi$  and  $N_s = 20$ . We see that with increasing  $u$  and therefore nonlinearity, current oscillations become larger and more chaotic and eventually average to zero over time for large  $u$ , as we will see in the next section. The notion of  $t_c$  does not make sense in this case since no additional energy scale appears to be associated with real parts of eigenvalues.

### C. Time-averaged circular current and coherence

We now evaluate the time-averaged circular current numerically,

$$\langle I(\theta_0) \rangle = \lim_{T \rightarrow \infty} \frac{1}{T} \int dt I(\theta_0), \quad (27)$$

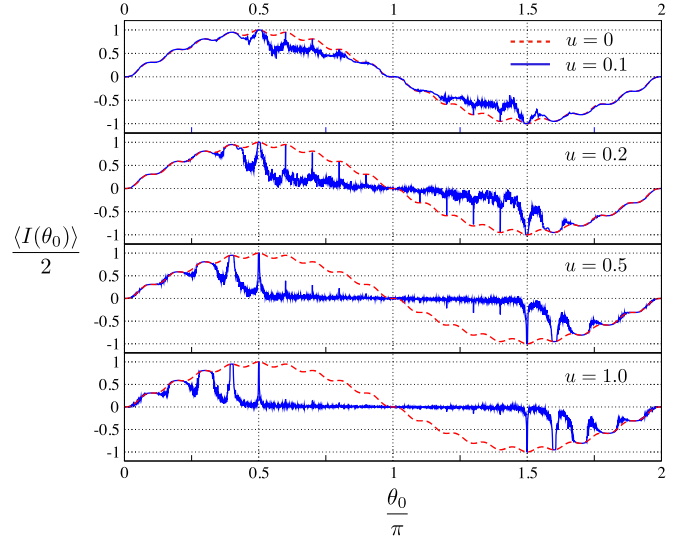


FIG. 11. Time-averaged circular current normalized by its maximum value ( $=2$ ) versus the initial phase difference  $\theta_0$ . The current is calculated for an  $N_s = 20$  ring and four different values of  $u$ , as indicated in the panels. The red dashed lines correspond to the  $u = 0$  noninteracting case and is used as a reference; the blue solid lines correspond to the interacting systems. The current is averaged over the time interval  $t \in [0, 200]$ .

for initial conditions (15) with  $\theta_0$  ranging from 0 to  $2\pi$ , covering stable and unstable regions of the stability diagram in full. We chose a ring with  $N_s = 20$  sites and four values of  $u$  greater than the maximum  $u_c$  listed in Table I. Given the discussion about  $t_c$  in the previous section, it is clear that the resulting time-averaged current for the discrete unstable modes will depend on the numerically available time interval, over which we can let our program run, providing reliable results. In our case  $t \in [0, 200]$ . The results for the averaged current are presented in Fig. 11. The four panels in Fig. 11 correspond to four different values of  $u$ , as indicated. The dashed curve is the current for  $u = 0$  and is shown in all the panels for reference. For small values of the dimensionless interaction  $u = 0.1$  the deviations of the current from  $u = 0$  values in the stable part of the plot are hardly visible (i.e., for  $\theta_0 \in [0, \pi/2]$  and  $[3\pi/2, 2\pi]$ ). For the unstable part,  $\theta_0 \in (\pi/2, 3\pi/2)$ , it is striking that  $t_c$  is, in fact, greater than 200; otherwise, the averaged current at the unstable discrete modes remains unaffected by the chaotic regime even though  $u > (u_c)_{\text{max}}$ . Since there are no additional timescales for  $\theta_0$  in between the discrete modes, the average current values begin to deviate from their  $u = 0$  values due to chaotic dynamics (see Fig. 10).

Upon increasing interaction,  $t_c$  decreases, so that for  $u = 0.2$  the value of  $t_c$  becomes of the order of 180, which is comparable to the maximum value of  $t$  in our numerics. As a result, the current values for discrete unstable modes remain practically unaffected, whereas the in-between  $\theta_0$  correspond to circular currents quickly averaging out to zero. This effect is also visible around the stability boundaries  $\theta_0 = \pi/2$  and  $\theta_0 = 3\pi/2$ . Although current values at stable discrete modes remain constant, the values in between begin to feel the effect of the increasing interaction. These tendencies become

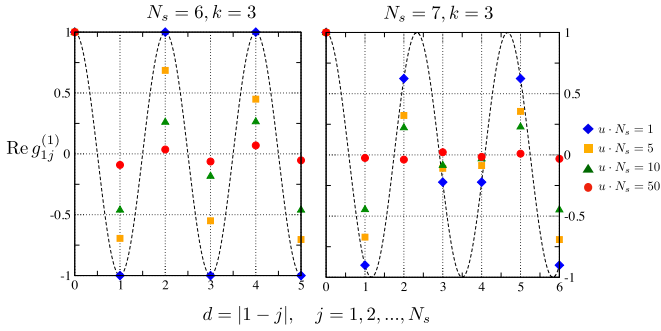


FIG. 12. The real part of the first-order correlation function  $\text{Re } g_{ij}^{(1)}$  averaged over time in the interval  $t \in [0, 200]$ . The correlation function is plotted as a function of distance with respect to the first site (the distance is normalized by a lattice constant  $a \equiv 1$ ).

more pronounced as we increase the interaction further. As  $t_c$  rapidly decreases ( $t_c \sim 75$  for  $u = 0.5$  and  $t_c \sim 35$  for  $u = 1$ ), so does the time-averaged current in the unstable region. For  $u = 1$ , this current is practically zero everywhere in the unstable region. The stable region is less affected by interaction, and the effect is most visible for values of  $\theta_0$  falling between the stable discrete modes, close to the stability boundaries. In the limit of large  $N_s$ , the unstable modes fill the interval  $(\pi/2, 3\pi/2)$ , while the stable modes fill the intervals  $[0, \pi/2]$  and  $[3\pi/2, 2\pi]$ . Large  $N_s$  approaches the continuous limit where all  $\theta_0$  are eigenmodes (because  $\theta_0^k$  merge together). The current in the limit of large  $N_s$  is described by  $2 \sin \theta_0$ , but in the unstable region the current averages to zero above  $u_c$ , provided the averaging time period is greater than  $t_c$ .

The circular current averaging to zero is equivalent to a loss of coherence in the system. The coherence can also be quantified by the first-order coherence function

$$g_{ij}^{(1)} = \frac{\langle \psi_i^* \psi_j \rangle}{\sqrt{\langle |\psi_i|^2 \rangle \langle |\psi_j|^2 \rangle}}. \quad (28)$$

It can be experimentally measured by interferometry as a function of the distance from a fixed site. In Fig. 12 we show the real part of the coherence function versus distance from site  $i = 1$ . We chose two different initial values of the phase difference:  $\theta_0^{(3)}$  for  $N_s = 6$ , i.e., the  $\pi$  mode of a six-site ring, and a mode  $\theta_0^{(3)}$  close to  $\pi$  of a seven-site ring. Although both of these modes are unstable, experiments on polariton condensates [19] demonstrate nonzero circulating currents and coherence corresponding to small values of  $u$ , e.g.,  $uN_s = 1$  in Fig. 12. This means that either the interaction was rather small in the experiment and  $t_c$  was relatively large or there were other stabilizing factors in the experimental system. For example, the experimental system is an open system, whereas our system is closed.

In Fig. 12 we further demonstrate how the coherence is destroyed by interaction and averages to zero for increasing  $u$  (see data for  $uN_s = 10$  and  $uN_s = 50$ ).

## V. CONCLUSIONS AND DISCUSSION

We analyzed circular currents and their stability in rings of condensates under specific initial conditions of equal filling and homogeneous phase differences. We found a set of dis-

crete eigenmodes (phase differences) differentiated by their winding numbers. When such a mode falls into the interval  $(\pi/2, 3\pi/2)$ , it is stable until the interaction exceeds a certain value  $u_c$ . This critical interaction depends on the mode and on the ring size. When  $u_c$  is exceeded, the system dynamics and the circular current become chaotic, with the current quickly averaging to zero over time. This marks the effective loss of coherence in the system. We showed that this dephasing occurs not immediately upon entering the unstable regime but rather after a chaos onset period  $t_c$ . This is the time the system spends in its former stable orbit before exponentially sliding off into a chaotic trajectory. The timescale  $t_c$  can be arbitrarily large when the system is close to the stability boundary, i.e., when the unstable mode under consideration is close to  $\pi/2$  or  $3\pi/2$  or when  $u$  is close to  $u_c$ . For modes close to the antiphase  $\pi$  mode in the instability region, i.e., for modes falling in the interval  $[\pi, \pi \pm 0.2\pi]$ , one can even establish a universal behavior of  $t_c \approx 28(u - u_c)^{-0.69}$ .

We also established that the critical time for chaos onset, that is, the dephasing time, is proportional to but about two orders of magnitude larger than the timescale of exponential deviations,  $1/\alpha$ , where  $\alpha$  is the current instability exponent. This may be relevant for technological applications of quantum coherent dynamics of rings of interacting Bose-Einstein condensates. The presence of the large chaos onset period  $t_c$  explains why in previous works about three-site condensate rings, the circular current was nonvanishing in the chaotic regime. It may also shed light on recent experimental observations of circulating currents in loops of polaritonic condensates with large winding numbers, although there can be other stabilizing factors.

In the future, it would be interesting to explore how fluctuations would affect the present description, and extension of this work to polaritonic condensates would be of interest. Another line of research could be to study condensate mixtures and their mutual coherence [25].

## ACKNOWLEDGMENTS

We acknowledge S. Ray and especially M. Eschrig for many fruitful discussions regarding the project. We are also grateful to an anonymous referee for their excellent comments which helped us improve the manuscript. This work was financially supported in part (J.K.) by the Deutsche Forschungsgemeinschaft (DFG) via SFB/TR 185 (277625399) and the Cluster of Excellence ML4Q (EXC 2004/1-390534769).

## APPENDIX A: EXACT SOLUTION OF THE NON-INTERACTING CASE

The noninteracting case when  $u = 0$  in Eq. (4) can be solved analytically by rewriting these simultaneous equations in matrix form, although it cannot be written in a succinct final solution for  $\psi$  due to the large number of unknown coefficients. However, with the simplifications  $\hbar \equiv 1$ ,  $E_i \equiv E_0$ ,  $U_i \equiv U$ , and  $K_{i,i+1} \equiv K$  for  $i = 1, \dots, N_s$  and expressing the time argument  $t$  in units of  $1/K$ , we get

$$i \frac{\partial}{\partial t} \vec{\psi}(t) = \hat{H} \vec{\psi}(t), \quad (A1)$$



where  $\epsilon = E_0/K$ , the vector  $\vec{\psi} = (\psi_0, \psi_1, \dots, \psi_{N_s-1})$  contains  $N_s$  condensate functions which are numbered from 0 to  $N_s - 1$  for convenience, and  $\hat{H}$  is an  $N_s \times N_s$  matrix,

$$\hat{H} = \begin{pmatrix} \epsilon & -1 & 0 & 0 & \dots & 0 & -1 \\ -1 & \epsilon & -1 & 0 & \dots & 0 & 0 \\ 0 & -1 & \epsilon & -1 & \dots & 0 & 0 \\ & & & \ddots & & & \\ 0 & 0 & 0 & 0 & \dots & \epsilon & -1 \\ -1 & 0 & 0 & 0 & \dots & -1 & \epsilon \end{pmatrix}. \quad (\text{A2})$$

This matrix is circulant and real symmetric with real eigenvalues (in our case, coinciding with energy eigenvalues). The eigenvectors  $\vec{v}$  of circulant matrices are well known and do not depend on circulant matrix entries [26]. The  $k$  component of  $\vec{v}$ , corresponding to an eigenvalue  $\lambda_j$ , reads

$$v_k(\lambda_j) = \exp i \frac{2\pi jk}{N_s}. \quad (\text{A3})$$

Here indices  $k, j = 0, 1, \dots, N_s - 1$ . The eigenvalues of  $\hat{H}$  are also readily found, as they are the discrete Fourier transforms of the first row of the matrix  $\hat{H}$ ,

$$\lambda_j = \sum_{k=0}^{N_s-1} h_{0k} \exp i \frac{2\pi jk}{N_s}, \quad (\text{A4})$$

where  $h_{00}, h_{01}, \dots, h_{0,N_s-1}$  are the entries of the first row of the circulant matrix (A2). In our case the eigenvalues acquire the simple form

$$\lambda_j = \epsilon - 2 \cos \left( \frac{2\pi j}{N_s} \right). \quad (\text{A5})$$

This gives us the general solution

$$\psi_n(t) = \sum_{j=0}^{N_s-1} c_j v_n(\lambda_j) e^{-i\lambda_j t}, \quad (\text{A6})$$

where the coefficients  $c_j$  are defined by initial values of the condensate wave functions  $\vec{\psi}(0)$ ,

$$\vec{\psi}(0) = \hat{F} \vec{c}, \quad (\text{A7})$$

where the discrete Fourier transform matrix  $\hat{F}$  contains eigenvectors  $\vec{v}(\lambda_j)$  as columns

$$F_{kj} = v_k(\lambda_j), \quad (\text{A8})$$

with  $k, j = 0, 1, \dots, N_s - 1$ .  $\vec{c}$  is hence determined by the inverse Fourier transform

$$c_j = \frac{1}{N_s} \sum_{k=0}^{N_s-1} e^{-i \frac{2\pi}{N_s} k \cdot j} \psi_k(0). \quad (\text{A9})$$

Finally,

$$\psi_n(t) = \frac{1}{N_s} \sum_{j,k=0}^{N_s-1} e^{i \frac{2\pi}{N_s} (n-k)j} \psi_k(0) e^{-i\lambda_j t}. \quad (\text{A10})$$

For the particle number per site  $N_n = \psi_n \psi_n^*$  we get

$$N_n = \sum_{j,k=0}^{N_s-1} c_{n,j,k} e^{-it(\lambda_j - \lambda_k)}, \quad (\text{A11})$$

$$c_{n,j,k} = \frac{1}{N_s^2} \sum_{l,m=0}^{N_s-1} e^{i \frac{2\pi}{N_s} (n-k-l+m)j} \psi_l(0) \psi_m^*(0). \quad (\text{A12})$$

As an example, we present solutions for  $N_s = 3$ . The eigenvalues are  $\lambda_1 = \lambda_2 = \epsilon + 1$  and  $\lambda_3 = \epsilon - 2$ , and the three wave functions have the form

$$\psi_i(t) = \frac{S}{3} e^{i(2-\epsilon)t} + \left( \psi_i(0) - \frac{S}{3} \right) e^{-i(\epsilon+1)t}, \quad S = \sum_{i=1}^3 \psi_i(0). \quad (\text{A13})$$

The occupation number per site is then

$$n_i = n_i(0) + 2\text{Re} \left[ \frac{S}{3} \left( \psi_i^*(0) - \frac{S^*}{3} \right) (e^{3it} - 1) \right]. \quad (\text{A14})$$

For initial conditions (15) and  $\theta_0$  coinciding with the eigenmodes (17),  $S = 0$ , giving the simple expressions

$$\psi_i(t) = \psi_i(0) e^{-i(\epsilon+1)t}, \quad n_i(t) = n_i(0) = 1. \quad (\text{A15})$$

## APPENDIX B: LINEAR STABILITY ANALYSIS OF THE INTERACTING SYSTEM

Equations (8) are real equations describing the dynamics of an interacting system. In order to analyze their linear stability we construct the Jacobian matrix for  $2N_s$  variables  $n_1, n_2, \dots, n_{N_s}, \varphi_1, \varphi_2, \dots, \varphi_{N_s}$ ,

$$J = \begin{pmatrix} \frac{dn_1}{dn_1} & \dots & \frac{dn_1}{d\varphi_{N_s}} \\ \vdots & \ddots & \vdots \\ \frac{d\varphi_{N_s}}{dn_1} & \dots & \frac{d\varphi_{N_s}}{d\varphi_{N_s}} \end{pmatrix}, \quad (\text{B1})$$

where  $\varphi_i = \theta_{i,i+1}$ .

Fixed points are determined from the steady-state condition of Eqs. (8),

$$x = n_i = 1, \quad y = \varphi_i = \frac{2\pi}{N_s} k, \quad i, k = 1, \dots, N_s. \quad (\text{B2})$$

The Jacobian matrix  $J$  at the fixed points can be written as a  $2 \times 2$  block matrix,

$$J = \begin{pmatrix} S & C \\ D & S \end{pmatrix}. \quad (\text{B3})$$

Here the matrices  $S, C$ , and  $D$  are circulant  $N_s \times N_s$  matrices, whose elements can be written as

$$\begin{aligned} S_{ij} &= \sin(y)(\delta_{i,j-1} - \delta_{i,j+1}), \\ C_{ij} &= 2x \cos(y)(-\delta_{i,j} + \delta_{i,j-1}), \\ D_{ij} &= \left( u + \frac{3 \cos(y)}{2x} \right) (\delta_{i,j} - \delta_{i,j+1}) \\ &\quad + \frac{\cos(y)}{2x} (\delta_{i,j+2} - \delta_{i,j-1}). \end{aligned} \quad (\text{B4})$$

We see that only the  $D$  matrix depends on the interaction  $u$ . All circulant matrices of the same size have the same eigenvectors; thus, all circular matrices of the same size can be

diagonalized by  $J_S = U^{-1}SU$ , where the  $U$  matrix columns are the circulant matrix eigenvectors. Using the rules for inverses of block matrices, we perform a simple transformation to diagonalize the circulant matrices in the Jacobian matrix:

$$\begin{pmatrix} U^{-1} & 0 \\ 0 & U^{-1} \end{pmatrix} \begin{pmatrix} S & C \\ D & S \end{pmatrix} \begin{pmatrix} U & 0 \\ 0 & U \end{pmatrix} = \begin{pmatrix} J_S & J_C \\ J_D & J_S \end{pmatrix}. \quad (\text{B5})$$

A similar transformation preserves the eigenvalues, and the  $J_S$ ,  $J_C$ , and  $J_D$  matrices are now diagonal matrices. As all of the new diagonal matrices commute, we can take advantage of a block-matrix determinant rule to find the eigenvalues of  $J$ :

$$\text{Det} \begin{pmatrix} J_S - \lambda I & J_C \\ J_D & J_S - \lambda I \end{pmatrix} = \text{Det}[(J_S - \lambda I)^2 - J_D J_C] = 0. \quad (\text{B6})$$

This equation can be rewritten as

$$(\lambda_j^S - \lambda_j)^2 - \lambda_j^D \lambda_j^C = 0, \quad j = 1, \dots, N_s, \quad (\text{B7})$$

where  $\lambda_j^S$ ,  $\lambda_j^C$ , and  $\lambda_j^D$  are the eigenvalues of  $S$ ,  $C$ , and  $D$ , respectively, and  $\lambda_j$  is the eigenvalue of the Jacobian  $J$ . We get

$$\lambda_j = \lambda_j^S \pm \sqrt{\lambda_j^D \lambda_j^C}, \quad j = 1, \dots, N_s. \quad (\text{B8})$$

Now we collect the eigenvalues of the circulant matrices  $S$ ,  $C$ , and  $D$ , which can be found following the method ex-

plained in Appendix A:

$$\begin{aligned} \lambda_j^S &= -2i \sin(y) \sin\left(\frac{2\pi j}{N_s}\right), \\ \lambda_j^C &= 2x \cos y \left( \exp -i \frac{2\pi j}{N_s} - 1 \right), \\ \lambda_j^D &= \left( u + \frac{3 \cos(y)}{2x} \right) \left( 1 - \exp i \frac{2\pi j}{N_s} \right) \\ &\quad + \frac{\cos(y)}{2x} \left( \exp i \frac{4\pi j}{N_s} - \exp -i \frac{2\pi j}{N_s} \right). \end{aligned} \quad (\text{B9})$$

As a result we get for  $\lambda_j = \lambda_j(k)$

$$\begin{aligned} \lambda_j(k) &= 2i \left\{ -\sin \theta_0^k \sin\left(\frac{2\pi j}{N_s}\right) \right. \\ &\quad \left. \pm \sin\left(\frac{\pi j}{N_s}\right) \sqrt{2 \cos \theta_0^k \left[ 2 \cos \theta_0^k \sin^2\left(\frac{\pi j}{N_s}\right) + u \right]} \right\}, \end{aligned} \quad (\text{B10})$$

The eigenvalues are purely imaginary if the expression under the square root is non-negative for all  $j$ . This corresponds to a neutral center and stable system. If at least one of the eigenvalues acquires a real part, there would be an exponential instability in the system. We discuss this in more detail in the main text after Eq. (18).

- 
- [1] T. L. Gustavson, P. Bouyer, and M. A. Kasevich, Precision Rotation Measurements with an Atom Interferometer Gyroscope, *Phys. Rev. Lett.* **78**, 2046 (1997).
- [2] B. P. Anderson and M. A. Kasevich, Macroscopic quantum interference from atomic tunnel array, *Science* **282**, 1686 (1998).
- [3] D. W. Hallwood, T. Ernst, and J. Brand, Robust mesoscopic superposition of strongly correlated ultracold atoms, *Phys. Rev. A* **82**, 063623 (2010).
- [4] L. Amico, D. Aghamalyan, F. Auzsotol, H. Crepaz, R. Dumke, and L. C. Kwek, Superfluid qubit systems with ring shaped optical lattices, *Sci. Rep.* **4**, 4298 (2014).
- [5] D. Aghamalyan, M. Cominotti, M. Rizzi, D. Rossini, F. Hekking, A. Minguzzi, L. C. Kwek, and L. Amico, Coherent superposition of current flows in an atomtronic quantum interference device, *New J. Phys.* **17**, 045023 (2015).
- [6] G. Arwas and D. Cohen, Chaos and two-level dynamics of the atomtronic quantum interference device, *New J. Phys.* **18**, 015007 (2016).
- [7] C. Ryu, P. W. Blackburn, A. A. Blinova, and M. G. Boshier, Experimental Realization of Josephson Junctions for an Atom SQUID, *Phys. Rev. Lett.* **111**, 205301 (2013).
- [8] M. Tsubota and K. Kasamatsu, Josephson current flowing in cyclically coupled Bose-Einstein condensates, *J. Phys. Soc. Jpn.* **69**, 1942 (2000).
- [9] K. Kasamatsu and M. Tsubota, Vortex generation in cyclically coupled superfluids and the Kibble-Zurek mechanism, *J. Low Temp. Phys.* **126**, 315 (2002).
- [10] D. R. Scherer, C. N. Weiler, T. W. Neely, and B. P. Anderson, Vortex Formation by Merging of Multiple Trapped Bose-Einstein Condensates, *Phys. Rev. Lett.* **98**, 110402 (2007).
- [11] Gh.-S. Paraoanu, Persistent currents in a circular array of Bose-Einstein condensates, *Phys. Rev. A* **67**, 023607 (2003).
- [12] E. T. D. Matsushita and E. J. V. de Passos, Stability of Bose-Einstein condensates in a circular array, [arXiv:0909.0920](https://arxiv.org/abs/0909.0920).
- [13] C. Arwas and D. Cohen, Chaos, metastability and ergodicity in Bose-Hubbard superfluid circuits, in *Nuclei and Mesoscopic Physics 2017*, AIP Conf. Proc. No. 1912 (AIP, Melville, NY, 2017), p. 0200001.
- [14] C. Arwas and D. Cohen, Monodromy and chaos for condensed bosons in optical lattices, *Phys. Rev. A* **99**, 023625 (2019).
- [15] C. Arwas and D. Cohen, Superfluidity in Bose-Hubbard circuits, *Phys. Rev. B* **95**, 054505 (2017).
- [16] K. Nemoto, C. A. Holmes, G. J. Milburn, and W. J. Munro, Quantum dynamics of three coupled atomic Bose-Einstein condensates, *Phys. Rev. A* **63**, 013604 (2000).
- [17] J. Dziarmaga, M. Tylutki, and W. H. Zurek, Ring of BEC pools as a trap for persistent flow, *Phys. Rev. B* **84**, 094528 (2011).
- [18] S. Moulder, S. Beattie, R. P. Smith, N. Tammuz, and Z. Hadzibabic, Quantized supercurrent decay in an annular Bose-Einstein condensate, *Phys. Rev. A* **86**, 013629 (2012).
- [19] T. Cookson, K. Kalinin, H. Sigurdsson, J. Töpfer, S. Alyatkin, M. Silva, W. Langbein, N. G. Berloff, and P. G. Lagoudakis, Geometric frustration in polygons of polariton condensates

- creating vortices of varying topological charge, *Nat. Commun.* **12**, 2120 (2021).
- [20] F. S. Cataliotti, S. Burger, C. Fort, P. Maddaloni, F. Minardi, A. Trombettoni, A. Smerzi, and M. Inguscio, Josephson junction arrays with Bose-Einstein condensates, *Science* **293**, 843 (2001).
- [21] A. Smerzi, S. Fantoni, S. Giovanazzi, and S. R. Shenoy, Quantum Coherent Atomic Tunneling between Two Trapped Bose-Einstein Condensates, *Phys. Rev. Lett.* **79**, 4950 (1997).
- [22] A. Trombettoni and A. Smerzi, Discrete Solitons and Breathers with Dilute Bose-Einstein Condensates, *Phys. Rev. Lett.* **86**, 2353 (2001).
- [23] A. Smerzi, A. Trombettoni, P. G. Kevrekidis, and A. R. Bishop, Dynamical Superfluid-Insulator Transition in a Chain of Weakly Coupled Bose-Einstein Condensates, *Phys. Rev. Lett.* **89**, 170402 (2002).
- [24] M. Trujillo-Martinez, A. Posazhennikova, and J. Kroha, Nonequilibrium Josephson Oscillations in Bose-Einstein Condensates without Dissipation, *Phys. Rev. Lett.* **103**, 105302 (2009).
- [25] A. Richaud and V. Penna, Phase separation can be stronger than chaos, *New J. Phys.* **20**, 105008 (2018).
- [26] P. J. Davis, *Circulant Matrices*, 2nd ed. (Chelsea, New York, 1994).